Chapter 2

Experimental Methods

Several techniques were used for the production and analysis of the materials investigated in this thesis, and these will be described in this chapter. Firstly, the main methods used for the deposition of amorphous carbon and amorphous carbon nitride materials are discussed, namely the filtered cathodic arc and chemical vapour deposition. The various specimen preparation, measurement and analysis techniques used in characterisation of these materials specimens will then be described. These techniques include the preparation of Transmission Electron Microscopy (TEM) and Scanning Electron Microscopy (SEM) samples, the collection of Electron Energy Loss Spectroscopy (EELS) and Energy Filtered Electron Diffraction Patterns (EFDP), Plasmon Analysis and calculation of Reduced Density Functions.

2.1 Cathodic Arc Deposition

The cathodic arc is a vacuum arc used for the deposition of thin-film coatings from conductive target materials. The cathodic arc system consists of a solid "target" of one desired coating material, in a vacuum chamber, where there is a negative bias of approximately 20V between the target and chamber. Deposition occurs when an induced electrical arc (provided by an arc welding generator) generates a plasma. The

arc is activated by "striking" a trigger (electrically connected to the chamber) onto the target surface. The arc forms a continuous discharge at several points on the target which "walk" in a random fashion across the surface. The total current is about 100 A.

The discharge liberates ions with significant kinetic energy [1] from the surface. These are attracted to the grounded substrate some distance from the target. Cooling water circulated through the target mount (with which it is in thermal contact) prevents overheating of the target material.

A description of the *filtered* cathodic arc using a "curved-solenoid" first appeared in the work of Askenov *et al.* [2] who used the curved "optical" filter to prevent line-of-sight between the target and substrate. The filter removes the majority of "macro-particles" – minute flakes of target material liberated by the continuous arc discharge. The diagram fig (2.1) shows a schematic of the filtered cathodic arc deposition system as used in this work.

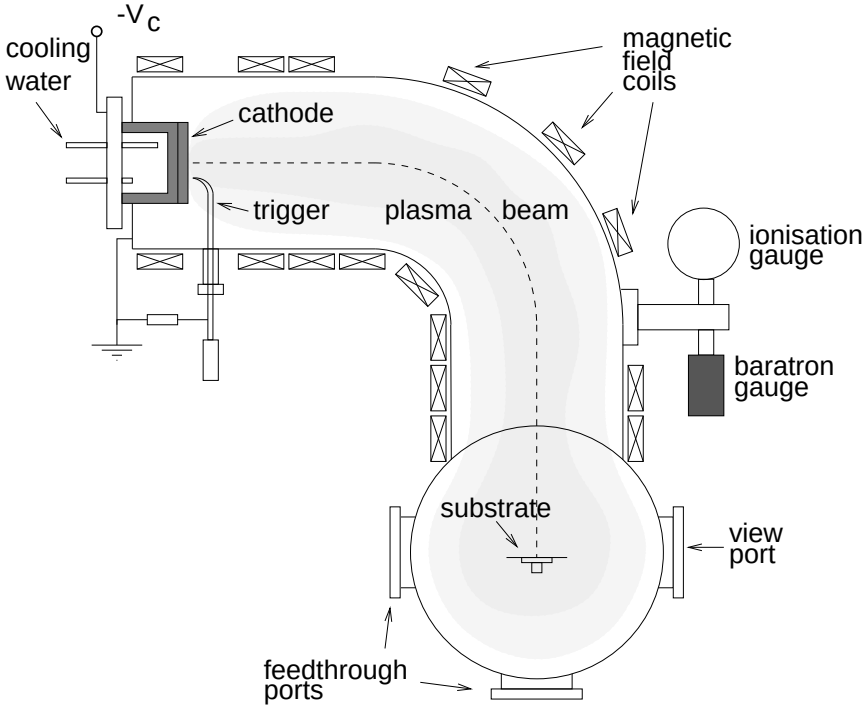

Figure 2.1: The filtered cathodic arc used for the production of films in this thesis. The un-filtered cathodic arc is similar in arrangement without the use of a curved-solenoid macro-particle filter. Reproduced with permission, Gerstner [3]

2.1.1 Ion Assisted Deposition in the filtered Cathodic Arc

The cathodic arc can be used to deposit a wide variety of materials derived from a conductive target. The arc is a flexible deposition system and parameters like substrate bias, temperature, vacuum pressure can be varied to deposit films of remarkably different properties [4]. The cathodic arc system also has the capability to "self-assist" ion deposition through a substrate bias.

With the addition of a gas to the deposition chamber [5] other atomic species can be deposited in tandem with the target material. For example, the addition of dry nitrogen gas with a carbon target enables amorphous carbon nitride with N^+ ion-assisted deposition.

In addition, binary or even ternary films can be deposited as the target can be made from practically any conducting material and gas mixtures are easily introduced into the vacuum system.

2.1.2 Deposition Parameters for $a-$C:N deposition

Carbon nitride films were deposited onto clean glass substrates using a cathodic arc system. In an attempt to increase both the deposition rate and the nitrogen retention in amorphous carbon-nitride films, an un-filtered cathodic arc system was used. The target material was graphite of 99·9% purity (Atomergic Chemicals). The chamber pressures of 20 and 50 mTorr (0·066 & 0·026 mbar) during deposition were controlled using a valve leading to a oil diffusion pumped secondary chamber.

Nitrogen doping of amorphous carbon was achieved by introducing pure nitrogen gas into the deposition chamber at a constant rate of 60 sccm. The cathodic arc deposition was performed in a series of short deposition runs separated by five minute cooling periods. It is considered unlikely the temperature of the substrate rose above 100°C during deposition, as the temperature of the substrate was checked after the final deposition.

2.2 Chemical Vapour Deposition of diamond and carbon nitride

As part of this program of study, a chance to collaborate with researchers at University of Melbourne and with Plasma Physics at Sydney University arose. The former collaboration involved deposition of diamond and $a-$C:N using an experimental HF-CVD apparatus, while the latter involved the deposition of diamond and $a-$C:N using an experimental microwave-CVD apparatus. In this section a description of the two types of apparatus will be presented.

2.2.1 Hot-filament CVD Deposition

The HF-CVD device consists of a quartz tube of about 5cm diameter, into which had been inserted two copper electrodes with a tungsten filament placed between - see fig (2.2). The tube was terminated at the top by a double-o-ring seal, with a small view port and gas inlet valve. The bottom of the tube contained a single o-ring sealed clamp through which was passed a specimen rod. On top of the specimen rod was a small flat-topped cap through which the thermocouple sensor protruded. Maximum substrate dimensions were about 1cm$\times$1cm.

Connected to the HF-CVD quartz tube was a rotary vacuum pump with associated needle valve and air inlets, a gas flow monitoring system (allowing three different metered gas flows simultaneously) and the current and voltage supply. External to the device was a Tempatie Series 8000 pyrometer for monitoring the filament temperature.

The substrate used for deposition was p-doped silicon <100> wafers. These are reasonably conductive (good for SEM), and are sufficiently thin to aid later sample preparation. All substrates and glassy carbon fragments were ultrasonically cleaned in pure ethanol mixed with diamond paste (0.3g of 4.5μm diamond paste with 30ml of EtOH) for 15 minutes. Silicon was bonded to the sample holder and a thermocouple sensor using carbon dag. The glassy carbon was placed on top of the silicon for deposition.

Before deposition, a tungsten filament is carburized in a 99%H_2/1%CH_4 mix for three

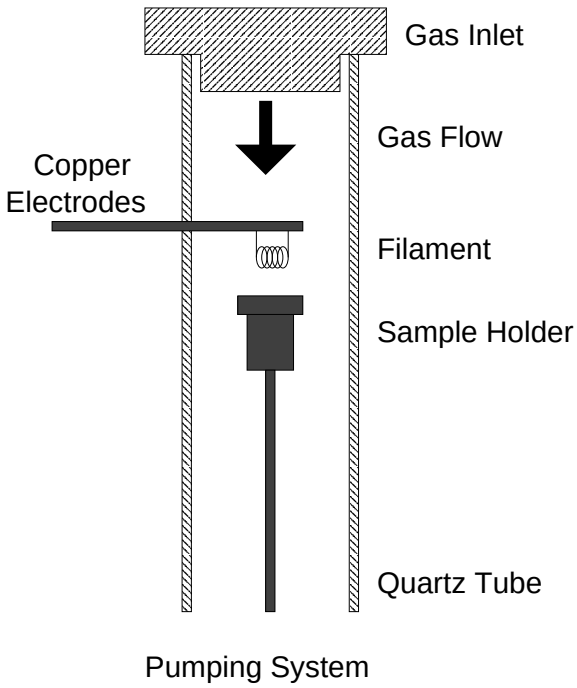

Figure 2.2: Schematic for hot-filament CVD deposition.

hours. After the carburization procedure a sample is placed in the chamber which is then evacuated to 30 Torr.

To enhance nucleation, the substrate is initially biased relative to the filament . A bias cage is also placed around the quartz tube and biased at the the electrode voltage (around 12V d.c.) to enhance flux confinement around the substrate. After about 30mins the bias to the substrate is switched off and normal deposition allowed to proceed for 180 mins. A number of samples were deposited under different bias, gas-mixture and pressure.

2.2.2 Microwave CVD Deposition

The microwave CVD deposition system consists of a cylindrical stainless steel reaction chamber attached to a rectangular-to-circular waveguide, an impedance matching system and a continuous 600W 2.4 GHz microwave magnetron. Inside the chamber was a half-wave plate which could be adjusted to ensure a single excitation mode in

the chamber. The sample (a circular-cut <100> silicon substrate) rested atop a pillar which could be positioned underneath the plasma ball. An Tempatie Series 8000 optical pyrometer was aimed along the axis of the sample pillar to measure the sample temperature during deposition. Connected to the Microwave-CVD reaction chamber was a rotary vacuum pump with associated needle valve and air inlets, a gas flow monitoring system (allowing three different metered gas flows simultaneously), and a Blazers QMG 064 partial pressure gauge for measurement of component gases. To enhance nucleation, the silicon substrate is initially roughened with 4.5μm diamond paste and cleaned with EtOH before deposition.

2.3 Transmission Electron Microscopy

Transmission electron microscopy (TEM) is a versatile technique for imaging, diffraction and micro-characterisation using electron and photon spectroscopy. A conventional transmission electron microscope (CTEM) operating at 300kV can produce images with a point resolution of about 2Å. A good description of the CTEM can be found in Williams and Carter [6].

Electrons, even high energy electrons, have a very limited penetration depth in most materials. An electron with energy 100keV has a *mean free path* of $\lambda = 3{\cdot}7\times10^{-12}$m [7]. By exponential decay $I = I_0 e^{-t/\lambda}$ an electron beam must only traverse around 5λ before the beam intensity has fallen below 1%. Consequently TEM samples are very thin and 30–70nm is typical.

In a CTEM, the microscope projection lenses can be adjusted to allow either the image plane or the back focal plane of the objective lens to fall on the viewing screen. The back focal plane of the objective lens is known as the diffraction plane, and contains a Fourier transform of the electronic potential of the material sample. The study of this electron diffraction from the crystalline planes is a tool for probing the structure of materials and can be used to distinguish between crystalline phases, poly-crystalline and amorphous materials.

Another type of electron microscope is the Scanning Transmission Electron Microscope

or STEM. Unlike the CTEM where the electrons "illuminate" the specimen evenly at all times, in a STEM a narrow beam of electrons approximately 1nm wide is rastered across the specimen in a manner analogous to a Scanning Electron Microscope (SEM). Electrons transmitted through the specimen are collected on a detector further down the microscope column. The collected signal is rastered on a TV monitor at the same rate as the sample is scanned. Electrons can be collected using a bright field (on axis), dark field (annular detector), high angle annular dark field (HAADF) or EELS which together with X-ray analysis (energy dipersive or wavelength dispersive) or electron diffraction allows a comprehensive analysis of specimen chemical composition and structure.

In a crystalline material, incident electrons reflect from crystallographic planes following the Bragg Law of diffraction $n\lambda = 2dsin\theta$ where d is the inter-planar distance. A crystalline diffraction pattern contains bright dots reflecting the symmetry of the crystal around the direction of the electron beam.

For poly-crystalline materials, the diffraction pattern reflects the underlying disorder of the crystal structure. A poly-crystalline diffraction pattern forms a series of concentric rings with radii corresponding to an atomic spacing d, rotated about the "optic" axis.

An amorphous material diffraction pattern is formed by the combination of single atom scattering and some amount of underlying short-range order. Because the diffraction pattern in the case of an amorphous material is difficult to interpret, a radial density function can be used.

For this program of study the microscopes used were a Philips EM430 CTEM fitted a LaB_6 filament operating at 300kV (or 200kV for EELS) and a Gatan 666 EELS spectrometer. The second microscope used was a VG HB501 STEM operating at 100kV fitted with field-emission electron gun and a Gatan 666 EELS spectrometer. The SEM used was a Philips XL30 operating at 5-30kV with an ultrathin window Oxford EDX system.

2.3.1 Radial Density Function

The radial density function $\rho(r)$ is the probability of finding an atom centre at a distance r from another atom centre. Consequently $\int_0^{r_{max}} 4\pi r^2 \rho(r) dr = N/V$ the number density of atoms in a sample. The function $\rho(r)$ is useful because it reflects the local environment of an average atom, and gives the nearest-neighbour distances and coordination (as will be discussed later).

The radial density function $\rho(r)$ is actually one of a number of pair-correlation functions. Other useful pair correlation functions are defined in terms of $\rho(r)$. One example, the $g(r)$ is defined as

$$g(r) = \frac{\rho(r)}{\rho_0}, \tag{2.1}$$

in which ρ_0 is the average number density of atoms. Another function derived from $\rho(r)$ and used in the study of amorphous materials is $G(r)$ which reflects the variations from average density ρ_0 in a sample. The $g(r)$ is related to $G(r)$ the *reduced density function* by

$$\begin{aligned} G(r) &= 4\pi r^2(\rho(r) - \rho_0) = 4\pi r^2 \rho_0(\rho(r) - 1) \\ &= 4\pi r^2 \rho_0(g(r) - 1) \end{aligned} \tag{2.2}$$

$G(r)$ can be calculated from the Fourier transform of the diffracted intensity, which in the case of amorphous materials is in the form of a ring pattern about the central unscattered maximum like that shown in fig (2.3). To explain how the $G(r)$ is calculated from an electron diffraction pattern, an understanding of the underlying electron-scattering theory will be explained.

2.3.2 Electron Scattering Theory

Consider a fast electron scattered from a lone atom. The incident electron plane wave with wave vector $\mathbf{k}_0 = 2\pi/\lambda$ will be scattered by the coulombic potential of the atom, shown in fig(2.4). The scattered electron beam of wave vector $\mathbf{k}$ will have intensity $I(s)$ given by:

$$I(s) = f(s)f^*(s) \tag{2.3}$$

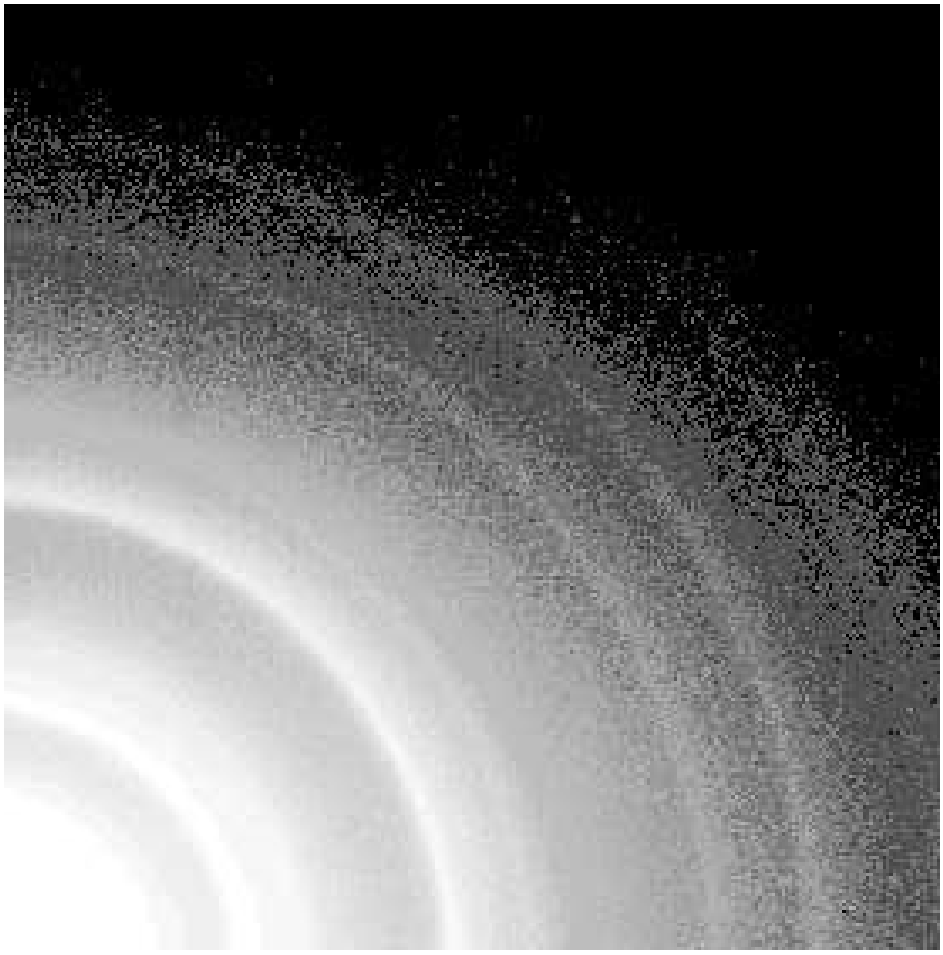

Figure 2.3: Part of a circular energy-filtered glassy carbon electron diffraction pattern collected on a Phillips 120 kV machine with a GIF[1]. The sample is a microtomed commercial V25 glassy carbon and has been energy filtered using the zero loss peak, with an 8eV window, image courtesy of Tim Petersen (RMIT).

where $f(s)$ is the *atomic* scattering factor defined as the three-dimensional Fourier transform of the atomic potential $\varphi(\mathbf{r})$ [8]:

$$f(s) = \int \varphi(\mathbf{r}) \mathbf{e}^{(2\pi i \mathbf{s}\cdot\mathbf{r})} dr \tag{2.4}$$

Within a material the atoms cannot be considered isolated and the scattering factor $\mathbf{F}(s)$ for the arrangement of atoms is the transform of the potential $\Phi(s)$ due to all the atoms:

$$\mathbf{F}(s) = \int \Phi(s) \mathbf{e}^{2\pi i \mathbf{s}\cdot\mathbf{r}} d\mathbf{r} \tag{2.5}$$

[1]Gatan Imaging Filter is a multiscanning charge coupled device (CCD) array 1024x1024 pixels.

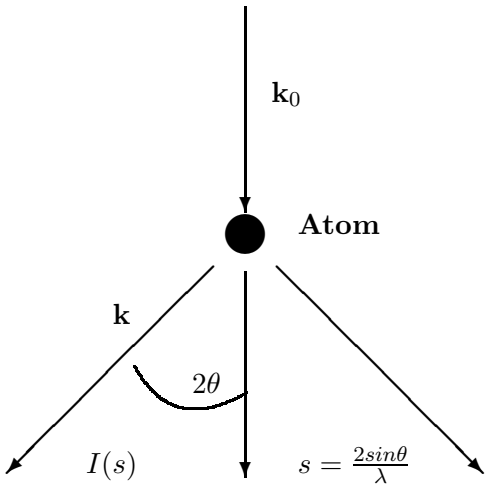

Figure 2.4: Scattering of an electron wave by an atom wave vector k_0

If we take a sufficiently large sample of N atoms from the material at positions r_i, a good approximation of the function $\Phi(r)$ is given by a summation of the atomic potentials $\varphi_i(\mathbf{r})$:

$$\Phi(\mathbf{r}) = \sum_{i=1}^{N} \varphi_i(\mathbf{r} - \mathbf{r_i}) \tag{2.6}$$

Replacing $\Phi(\mathbf{r})$ in Eq.(2.5) with Eq.(2.6) the scattering equation becomes:

$$F(s) = \sum_{i=1}^{N} \int \varphi(\mathbf{r} - \mathbf{r_i}) e^{(2\pi i \mathbf{s}\cdot\mathbf{r})} d\mathbf{r} \tag{2.7}$$

Using the notation $\mathbf{r'} = \mathbf{r} - \mathbf{r}_i$ we find:

$$F(s) = \sum_{i=1}^{N} e^{(2\pi i \mathbf{s}\cdot\mathbf{r}_i)} \int \varphi(\mathbf{r'}) e^{(2\pi i \mathbf{s}\cdot\mathbf{r'})} d\mathbf{r'} \tag{2.8}$$

The integral in Eq.(2.8) is identical to Eq.(2.4) the *atomic* scattering factor. This reduces Eq.(2.8) to:

$$F(s) = \sum_{i=1}^{N} f_i(s) e^{(2\pi i \mathbf{s}\cdot\mathbf{r}_i)} d\mathbf{r} \tag{2.9}$$

Following Eq.(2.3) the intensity of the scattered beam $I(s) = F(s)F^*(s)$, is therefore :

$$I(s) = \sum_{i=1}^{N} \sum_{j=1}^{N} f_i(s) f_j(s) e^{(2\pi i \mathbf{s}\cdot\mathbf{r}_{ij})} \tag{2.10}$$

where $\mathbf{r_{ij}} = \mathbf{r_i} - \mathbf{r_j}$. Eq.(2.10) is a generic expression for the scattered intensity from any arrangement of atoms. Because there are no assumptions about the symmetry of the arrangement, it can be used for crystalline, poly-crystalline or amorphous structures.

For materials containing just one type of atom, the atomic scattering factors $f_i(s)$ & $f_j(s)$ in Eq.(2.10) are identical. We can split the summation into terms where $i = j$ and $i \neq j$ and remembering $f_i(s) = f_j(s) = f(s)$ gives:

$$I(s) = Nf^2(s) + f^2(s)\sum_{i=1}^{N}\sum_{i\neq j}^{N} e^{(2\pi i \mathbf{s}\cdot\mathbf{r}_{ij})} \tag{2.11}$$

This reveals that the collected diffraction intensity is actually a summation of the atomic scattering factor $f(s)$ overlaid with the diffracted intensity due to the order in the material.

A density function $\rho(\mathbf{r}_{ij})$ is now introduced which measures probability density [2] as a function of $\mathbf{r}_{ij}$. The identity $\rho(\mathbf{r}_{ij})d\mathbf{V}_i$ will equal the total number of atoms in volume dV_i at r_{ij} from the ith atom.

Assuming the material is isotropic (the local environment for one atom is identical to any other), we can replace $\rho(\mathbf{r}_{ij})$ by $\rho(r_{ij})$:

$$I(s) = Nf^2(s) + f^2(s)\sum_{i=1}^{N}\int \rho(r_{ij})e^{(2\pi i \mathbf{s}\cdot\mathbf{r}_{ij})}dV_i \tag{2.12}$$

As the material is isotropic the integral in Eq.(2.12) is dependent only on $|r|$ not $\mathbf{r}$. By replacing $\mathbf{r}_{ij}$ and $\mathbf{r}$ by r and s we find:

$$I(s) = Nf^2(s) + f^2(s)\sum_{i=1}^{N}\int \rho(\mathbf{r})e^{(2\pi i s r)}d\mathbf{V} \tag{2.13}$$

Integrating over spherical coordinates (averaging) for angles $\theta = 0$ to 2π and $\phi = 0$ to π gives:

$$I(s) = Nf^2(s) + Nf^2(s)\int_0^\infty 4\pi r^2\rho(r)\frac{sin(2\pi i s r)}{2\pi s r}dr \tag{2.14}$$

Rearranging the equation to yield the density function as a function of collected intensity $I(s)$ a new function $\phi(s)$ the *reduced intensity function* is introduced:

$$\phi(s) = \frac{s\left(I(s) - Nf^2(s)\right)}{Nf^2(s)} \tag{2.15}$$

[2] the integral of the probability density for all r is $\int_0^\infty \rho(r_{ij})dV_i = N$, the number of atoms

So the *reduced intensity function* is given by:

$$\phi(s) = \int_0^\infty 2r\rho(r)sin(2\pi sr)dr \tag{2.16}$$

We can replace $\rho(r)$ by $\rho(r) = \rho(r) - \rho_0(r) + \rho_0(r)$ where $\rho_0(r)$ is the average density of the material.

$$\phi(s) = \int_0^\infty 2r[\rho(r) - \rho_0(r)]sin(2\pi sr)dr + \int_0^\infty 2r\rho_0(r)sin(2\pi sr)dr \tag{2.17}$$

The second term can be ignored as numerical integration has shown it only has significant values around $s = 0$, and does not contribute strongly to the $G(r)$ because of the presence of the unscattered beam $\mathbf{k}_0$.

The first term in Eq.(2.17) is in the form of a Fourier sine transform which can be inverted if the following transform pairs $f(x)$ & $g(\omega)$ are used:

$$f(x) = 4\pi \int_0^\infty f(x)sin(\omega x)dx \tag{2.18}$$

$$g(\omega) = \frac{1}{2\pi^2} \int_0^\infty g(\omega)sin(\omega x)d\omega \tag{2.19}$$

By identifying $g(\omega) = s\phi(s)$ and $f(x) = r(\rho(r) - \rho_0))$ within the first part of Eq.(2.17) allows the following to be written:

$$r(\rho(r) - \rho_0) = \frac{1}{2\pi^2} \int_0^\infty s\phi(s)sin(sr)ds \tag{2.20}$$

The $G(r)$ or *reduced* density function (RDF) can now be defined as:

$$G(r) = 4\pi r(\rho(r) - \rho_0)) \tag{2.21}$$

from the substitution $G(r)$ can now be written as:

$$G(r) = \frac{2}{\pi} \int_0^\infty s\phi(s)sin(s \cdot r)ds \tag{2.22}$$

The $G(r) = -4\pi r\rho_0$ for $r < 2a$, where a is the atomic radius.

Eq.(2.22) shows that once $\phi(s)$ is calculated from the collected intensity $I(s)$ it is relatively simple to calculate the RDF or $G(r)$. A example of the experimentally collected $G(r)$ for glassy carbon (a turbostratic graphite-like material) is shown in fig(2.5). The first three nearest neighbour peaks correspond to the first three bond lengths in a graphite plane.

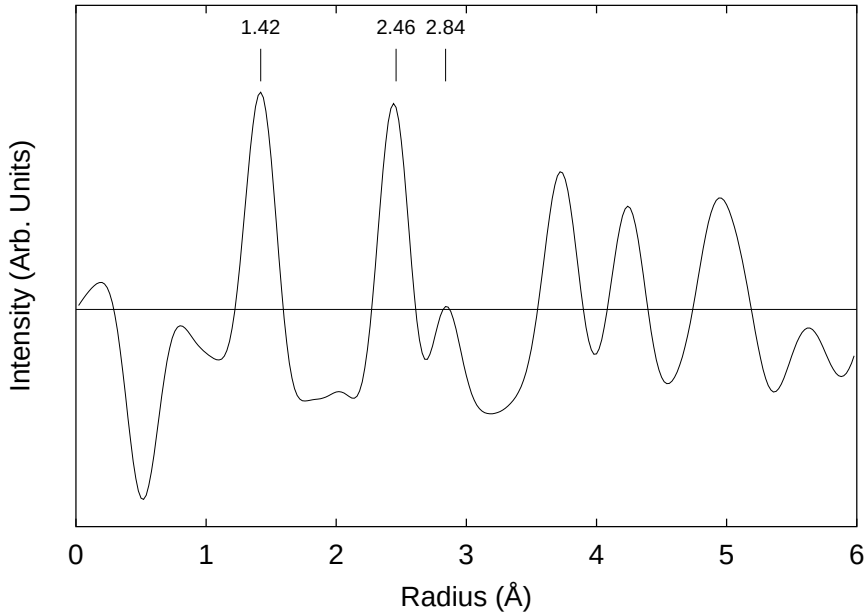

Figure 2.5: The experimental $G(r)$ for glassy carbon, collected in an EM430 at 300kV. The numbered labels represent the first three in-plane nearest neighbour distances for graphite.

If the sample contains two atomic types this technique gives a true G(r), but an assumption must be made. This assumption is that the atomic scattering factors of the two atomic types differs only by a multiplicative constant (i.e. f_i/f_j is constant in s). The procedure to find the RDF using this assumption is outlined in Cockayne and McKenzie [9]. Warren [10] outlines a more exact technique which does not use this assumption.

2.3.3 Calculation of Coordination Numbers

An important statistic for an amorphous network is the average coordination number C which is a measure of the number of nearest neighbours.

The average coordination number C_{ab}, the number of atoms falling within a spherical shell of inner radius r_a and outer radius r_b, for a structure is defined as:

$$C_{ab} = \int_{r_a}^{r_b} 4\pi r^2 \rho(r) dr \tag{2.23}$$

If we use Eq.(2.21)we can see that:

$$C_{ab} = \int_{r_a}^{r_b} rG(r)dr - \frac{4\pi}{3}\rho_0 \left(r_b^2 - r_a^2\right) \tag{2.24}$$

In a binary system it is difficult to interpret the coordination from this integral, and care should be used to ensure a clear definition of what is being measured.

2.3.4 Collection of the I(s)

In order to determine the I(s) from electron diffraction patterns so that a G(r) can be calculated as described above, it is a condition that the electrons contributing to the diffraction intensity are monochromatic. Therefore the diffraction pattern is energy-filtered by using either an microscope capable of energy filtered diffraction or a CTEM fitted with an energy-loss spectrometer (see Section 2.4).

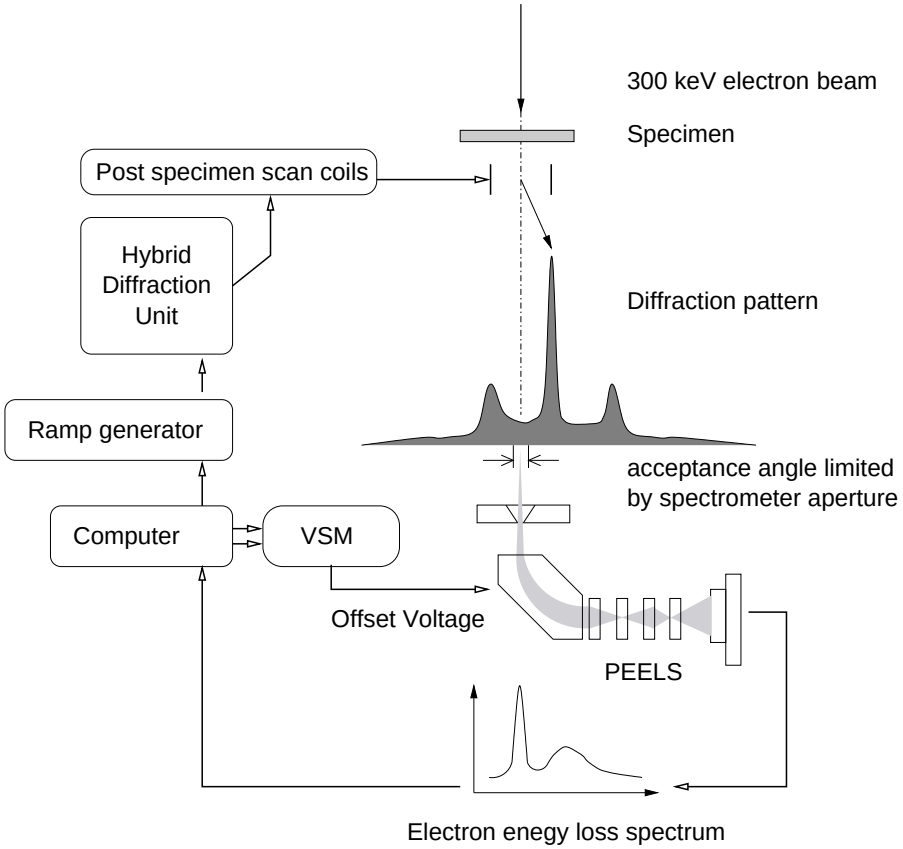

Figure 2.6: Schematic diagram of the energy-filtered electron diffraction pattern collection in a TEM .

The system used for collecting an energy-filtered electron diffraction patterns (EFDP)

in this thesis was discussed originally by Cockayne *et al.* [11] and Muller [12], with some more recent programming improvements of the collection software by McBride [13] and McCulloch [14]. The instrumentation used for the collection of EFDPs was the previously mentioned Philips EM430 TEM with a Gatan 666 PEELS Spectrometer attached operating at 300kV (see fig(2.10)).

A schematic of the EFDP collection system is shown below in fig(2.6) showing how the collection process is controlled through a computer collection card and a voltage scan module. During collection the diffraction pattern from the sample is passed over the EELS entry aperture in regular intervals using the Hybrid Diffraction Unit (HDU) scan coils and a low-loss EELS spectrum is collected. To reduce noise the spectrum is shifted off-axis in the spectrometer between collections using a Voltage Scan Module (VSM). The collected low-loss spectrum is top-hat filtered to remove plasmon contributions and the resulting diffraction pattern, $I(s)$ results. Top-hat filtering is the double derivative of the zero-loss peak (ZLP), and differs from the actual integrated intensity under a ZLP by a multiplicative constant.

During a collection of I(s) as the diffracted intensity fades at large s the integration time of the EELS spectrometer is increased. At each increase of the collection time the pattern re-collected to allow matching of the pattern. Fig(2.7) shows the as-collected experimental $I(s)$ for glassy carbon.

2.3.5 Calculation of reduced intensity function $\phi(s)$

The reduced intensity function $\phi(s)$ is related to the $I(s)$ by Eq.(2.15). The number of atoms N in the scattering volume is calculated by χ^2 fitting $f^2(s)$ to $I(s)$ at large s where the oscillations of $I(s)$ are small. Fig(2.7) shows the as-collected experimental $I(s)$ for glassy carbon and $Nf^2(s)$ fitted at large s. $\phi(s)$ the reduced intensity function is then calculated according to Eq.(2.15). The experimental $\phi(s)$ cfrom glassy carbon an be seen in fig(2.8a).

2.3.6 Damping of the ϕ(s)

The experimental $\phi(s)$ does not extend to infinite s, rather it is terminated at some value $s = s_{max}$ corresponding to some maximum scattering angle of the diffracted data collected in the I(s). The $G(r)$ in Eq.(2.22) will therefore be (in effect) convoluted with a step function in reciprocal space, equivalent to a sinc[3] function in real space. This real-space convolution decreases the resolution of the subsequent $G(r)$ calculation.

The loss of resolution in the $G(r)$ can be corrected for in the $\phi(s)$ by applying a damping factor, called *Lorsch* damping [12]:

$$G(r) = \frac{2}{\pi} \int_0^{s_{max}} s\phi(s)D(s)sin(s \cdot r)ds \tag{2.25}$$

where $D(s) = sin(s/s_{max})/(s/s_{max})$. The effect of the damping is shown in fig(2.8)(b), where an experimental $\phi(s)$ for glassy carbon is modified using Lorsch damping.

The experimental $G(r)$ for glassy carbon after Lorsch damping is shown in fig(2.5).

[3] sinc(x)=sin(x)/x

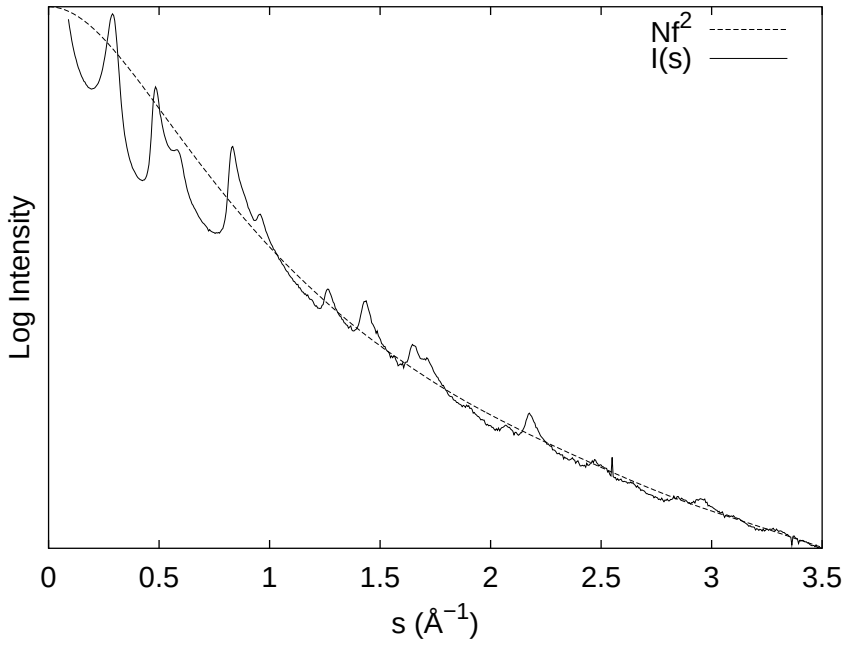

Figure 2.7: Experimental $I(s)$ and $Nf^2(s)$ for glassy carbon.

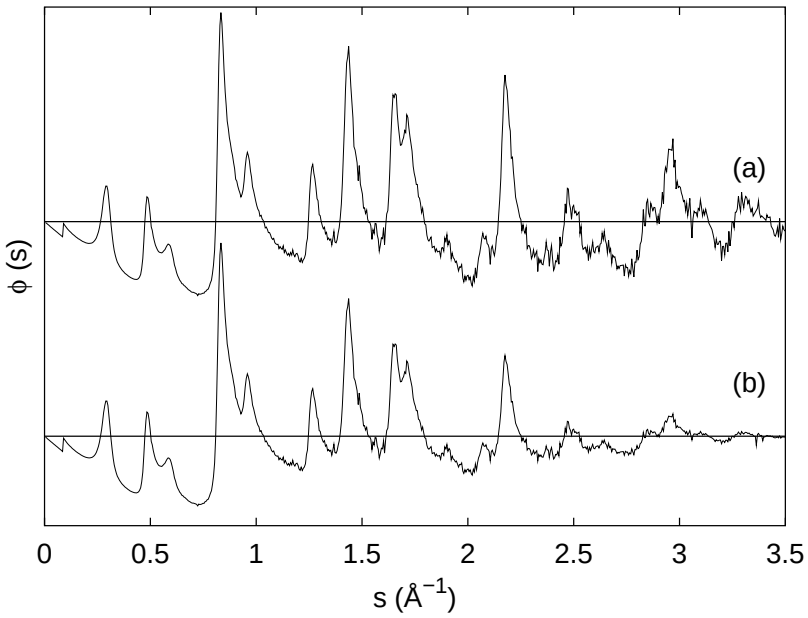

Figure 2.8: (a) Glassy carbon $\phi(s)$ as collected and calibrated against standard, (b) the same diffraction pattern with Lorsch damping (visible at high s)

2.3.7 Preparation of thin films samples for TEM analysis

Samples were prepared for TEM in three different ways, flotation, ultramicrotomy and ion-beam thinning. The flotation technique is used to prepare plan-view specimens. If glass substrates were used, these were pre-treated with a surfactant before deposition to assist in post-deposition film removal. The other two techniques were used for making cross-sectional samples of thin film for analysis.

For purposes of making cross-sectional samples, either small slivers of glassy carbon or polished silicon were attached to the substrates before the deposition of $a-$C and $a-$C:N. Glassy carbon substrates are used for Ultramicrotomy (see Section 2.3.7.2) as they can be sliced neatly with a diamond knife. Silicon substrates are used for Ion Beam Thinning (IBT) a method in which energetic ions are used to sputter away material from a "sandwich" of sample layers and substrate layers until only a thin electron transparent section remains (See Section 2.3.8).

2.3.7.1 Flotation Technique

As implied in the title, the flotation technique is the partial immersion of a deposited film sample with substrate into de-ionised water. Multiple fragments of the film are collected from the water surface using a small circle of steel wire. Sample fragments are transferred to a 3mm diameter copper grid (400 mesh) resting on laboratory grade filter paper for drying. The microscope specimens prepared in this manner were for plan-view TEM specimens.

2.3.7.2 Ultramicrotomy

One way of making cross-sectional samples for microscopy is the Ultramicrotomy technique. Originally pioneered for preparation of biological optical microscopy samples, Ultramicrotomy is very useful in the preparation of electron microscopy samples.

For this technique, triangular pieces of 100μm thick glassy carbon coated with either $a-$C or $a-$C:N were shattered and the pieces immured in a hard epoxy resin and baked overnight at 70°C. The next morning the resin block (measuring approx. 5x5x10mm) was carefully trimmed to reveal a small intrusion of glassy carbon in a plug of resin protruding from the main block. Taking a diamond knife, the resin/glassy carbon was carefully sliced to a thickness of approximately 70nm and ten to twenty samples collected onto copper grids.

2.3.8 Ion-Beam Thinning

IBT is a technique for the production of thin film samples for cross-section analysis in the TEM. First the substrate (generally silicon) is cleaved into four rectangular pieces of material. Two are glued face-to-face, the other two are placed sample side forming a block of four, with the area of interest innermost. Secondly the block of four samples is the attached to the base of a tripod-polisher and ground down until sufficiently thin to use in an ion beam thinner. Finally, attached to a "slot" type copper grid and placed in the ion-beam thinner, argon ions are fired at the sample until a laser directed down through the sample is detected beneath. The thinnest region formed is (hopefully) at the centre of the region of interest which can then be analysed using TEM.

2.4 Electron Energy Loss Spectroscopy

Electron energy loss spectroscopy (EELS) is a technique which collects electrons after passing through or reflecting from a sample and disperses them according to their energy. EELS was first used by Rydberg (1929) who reported on the energies of electrons reflected from the surface of a metal, and recorded that the loss spectrum was indicative of the chemical composition of the sample. Ruthemann [15] improved on the earlier work and recorded the first *transmission* energy loss spectrum of a thin film of Aluminium. EELS was first used for microanalysis by Hillier and Baker [16] in 1944 to record the K-edges for Silicon and Iron using an electron microprobe. The EELS tech-

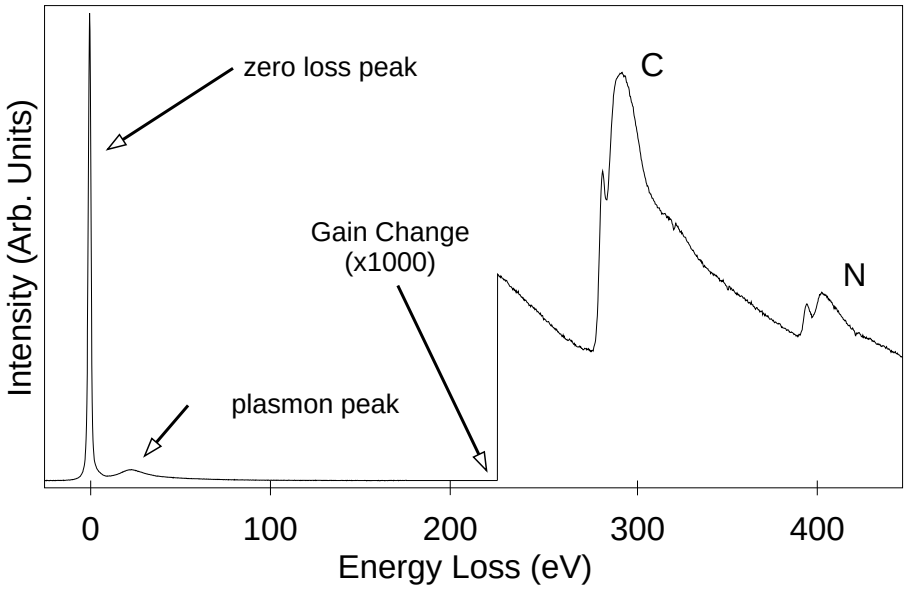

Figure 2.9: A typical EELS spectrum collected from a cathodic arc deposited amorphous carbon nitride, showing zero-loss peak, and carbon and nitrogen K-edge core loss events. The sample is approximately 70nm thick.

nique is ideal for the analysis of thin films containing low atomic number elements (for example carbon and nitrogen). EELS has an advantage over x-ray energy dispersive spectroscopy (EDS) for two reasons: x-ray flourescence and collection efficiency. X-ray flourescence efficiency (number of photons for each incident electron) for elements with $Z < 11$ is approximately 2% making elements such as carbon and nitrogen difficult to detect. Also, collection efficiency of 20 – 50% for EELS compared to about 1% for the isotropic emission of x-rays means beam currents need to be higher for a comparable

signal. The small sample thicknesses in TEM compared to SEM means EELS is a more efficient, versatile and sensitive technique. In a STEM, a small probe is used and spectra collected with extremely high spatial resolutions.

The form of EELS spectrometer used for this work collects electrons passing through a small aperture and then through a curved 90° magnetic filter. Taking the optical axis of the magnetic filter exit aperture as the Z direction, the electrons entering the filter are focused in the XY plane by the quadrupole magnets while evenly distributed in YZ plane. The focussed and dispersed electrons then impinge on a photodiode array (or in more modern devices, a CCD camera). The collected spectrum reveals inelastically scattered electrons as a function of energy loss as shown in fig (2.9). The particular model of spectrometer used in these studies was a Gatan 666 PEELS spectrometer (see fig(2.10) with a typical energy resolution of 1.6eV FWHM (200kV Philips EM430) and 0.8eV FWHM (100kV VG HB601 STEM). Looking at a representative energy loss spec-

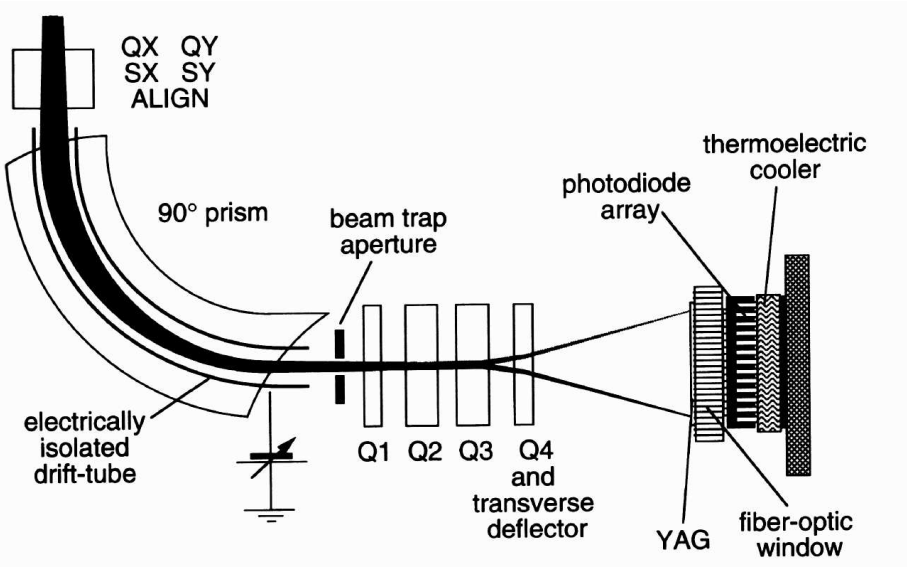

Figure 2.10: Schematic diagram of the Gatan 666 model Parallel Electron Energy-Loss Spectrometer (PEELS), showing pre-entry focusing and alignment coils, the 90° magnetic dispersing spectrometer, quadrupole magnet array (Q1-Q4) and Cesium - doped Yttrium Aluminium Garnet (YAG) scintillator fiber-optically coupled to the linear photodiode array. Reproduced from Egerton [17]

trum in Figure 2.9, the region of greatest intensity is the zero-loss or "elastic" peak. The energy-loss features between 5–50eV (low-loss region) result from the collective oscillation of valence electrons (plasmons) or interband transitions (eg. $\pi \Rightarrow \pi^*$). The low-loss region is useful for plasmon analysis which will be described later in Section 2.4.1.

Energy-loss features that fall in the range 50-1000eV are core-loss events, produced by the ionisation of an inner shell electron from an atom. The position of core-loss energy loss edges are therefore representative of the binding energy of the electron in the host atom and can be used for quantitative chemical identification. The overall shape of the core-loss feature is dependent on the principal quantum number (n) of the core-electron. Following the labeling of X-rays from electron shells, ionisation of an n=1 electron is referred to as a K-edge, similarly, n=2 is an L, n=3 an M, and do on and so forth. Table (2.1) lists the K, L and M edge energies for several elements including carbon and nitrogen.

Superimposed on each core-loss edge is fine-structure which alters the basic edge shape. The edge structure can be divided into two regions: energy loss near-edge structure (ELNES) and extended energy-loss fine structure (EXELFS). ELNES features are located within 50eV of the core-loss energy onset (binding energy), whereas EXELFS features are more than 50eV from edge-onset.

Fine structure arises because as the atom is ionised, the core electron's increased kinetic energy raises it to an un-occupied electron state in the material. This is expressed by the Bethe relation [17]:

$$\frac{d^2I}{d\Omega dE} = (\frac{2\pi}{\hbar})\rho(E)\left(\frac{e^2}{\varepsilon_0}\right)^2 \left|\frac{\langle f|exp(i\mathbf{q}\cdot r)|i\rangle}{q^2}\right|^2 \tag{2.26}$$

Where $|i>$ is the initial inner-shell electron wavefunction, $|f>$ the final unoccupied state of the atomic electron, $\rho(E)$ is the density of states for a final state electron with energy E and $\mathbf{q}$ is the magnitude of the momentum transfer given by $\hbar\mathbf{q} = \hbar(\mathbf{k_0} - \mathbf{k})$ (same as $\mathbf{s}$ previously defined). Core-loss edges features have a shape governed by two factors; the dipole selection rules which gives the basic profile; and the density of unoccupied states $\rho(E)$ which provides the fine structure.

Element	Plasmon (eV)	K-edge (eV)	L-edge (eV)
B (amorph.)	22.7	188	-
BN (hex)	9,26	188	-
BN (amorph)	24	188	-
C (diamond)	33.2	284	-
C (graphite)	27	284	-
C ($ta-$C)	29.5	284	-
C ($a-$C)	22	284	-
N	-	400	-
O	-	532	-
Na	5.7	1072	-
Al	15.0	1560	118
Si (crystal.)	16.7	1839	149
Si (amorph.)	16.3	1839	149
Si_3N_4 (α)	23.7	1839	149
Fe	23.0	7113	846
Cu	19.3	8979	951

Table 2.1: The plasmon, K-edge and L-edge energy loss values for a range of elements and compounds, reproduced from Egerton [17]

On the other hand, EXELFS is caused by the interference of the outgoing electron wave and the electron waves reflecting from surrounding atom potentials. In essence, the EXELFS features form a species-specific scattering function $S(Q)$ for the local environment. The EXELFS features can be used to form a $G(r)$ in much the same way as was described earlier assuming single scattering only is present, but this is generally only used in x-ray absorption spectroscopy because of the higher signal to noise in this technique.

The sampling of unoccupied density of states in the ELNES region of the core-loss spectrum can be treated in real space as the multiple-scattering of the outgoing spherical electron wavefunctions. This is the foundation of the theoretical Multiple Scattering

calculations covered in Chapter 5 of this thesis.

2.4.1 Quantitative Analysis using the Low Loss Region

As mentioned previously, electrons passing through a thin film sample undergo energy loss associated with either quasi-elastic or inelastic collision. One class of inelastic collisions is caused by a "group-excitation" of the loosely bound conduction electrons in the sample or *plasmon* losses.

The plasmon energy loss region falls between 0 – 40eV and the location of peaks depend on the free-electron density or plasma frequency of the material which is described by the following equation:

$$E_p = \hbar\omega_p \tag{2.27}$$

$$\omega_p^2 = \frac{N_e e^2 \rho}{\epsilon_o m_e^*} \tag{2.28}$$

where $\hbar$ is Plank's constant divided by 2π , m^* the effective mass, ω_p is the plasma frequency, N_e is the number density of electrons in the material and e is the charge on an electron. Although equations Eqn (2.27) and (2.28) are derived assuming a free-electron model they have proved good approximations for insulators [17].

For example the electron density for crystalline diamond is 3.53 x 10^{29} electrons/m^3. If the effective mass is taken as 0.55m_o, the plasmon frequency ω_p is 4.5 $\times$ $10^{16}s^{-1}$, giving a plasmon energy of 30eV. The experimentally observed plasmon energy of diamond is 33eV as listed in Table 2.1.

In practice, the plasmon energy (in eV) can be used to an estimate film density where the number of valence electrons per atom N_V is known or can be approximated. The mass density, ρ in g/cm^3 can be determined by:

$$\rho = \frac{M}{N_A} . \frac{E_p^2 \varepsilon_o m_e}{N_V \hbar^2} . 10^{-6} \tag{2.29}$$

where M is the molecular weight of the material in the film, N_A is Avagadro's Number, m_e is the mass of an electron and E_p the plasmon energy (in eV).

In this thesis the plasmon energy was measured by taking the first-derivative of the spectrum and measuring the energy at which the first derivative passes through zero.

2.4.2 Determination of sp^2 fractions using core-loss region

The ELNES of the core-loss edges contains information about the local bonding and order. One feature of the carbon K-edge from *sp* and sp^2 bonded carbon is the pre-edge $1s - \pi^*$ feature which arises from of π bonding in the sample.

The amount of sp^2 carbon in $a-$C and $a-$C:N is important to both its electronic and elastic properties. Measuring the relative intensity of $1s - \pi^\star$ transition to the $1s - \sigma^\star$ transitions was shown by Berger [18] to be indicative of the fraction of sp^2 (to sp^3) bonding. This is however, based on the assumption that the amount of *sp* bonding in $a-$C and $a-$C:N is negligible.

Recently McCulloch *et al.* [19] showed through the simulation of $a-$C using *ab initio* methods that there was a qualitative correlation between the integrated intensity of the 1s – π^* region in unoccupied density of states (DOS) and the sp^2 fraction at a range of densities of $a-$C and $ta-$C.

2.5 Elemental Concentrations using EELS

Elemental concentrations of atomic species in a sample can be measured from the integrated intensity beneath a core-loss feature in EELS. For this technique to be accurate, there are several corrections for plural scattering and/or multiple scattering which must be made.

2.5.1 Removal of plural scattering from core-loss edges

Plural scattering refers to electrons which experience more than one (experimentally resolvable) energy-loss event while traversing the specimen thickness. Plural scattering can drastically alter the observed shape of an inner-shell ionisation edge. The best technique for removal of plural scattering in the low-loss region is Fourier-Log deconvolution, while the technique of Fourier-Ratio is better employed on core-loss edges. To understand how to apply Fourier-Log and Fourier-Ratio deconvolution techniques the scattering of electrons in a solid will be discussed, followed by a description of each technique.

2.5.2 Effects of Multiple Scattering

The scattering of electrons through a sample can be treated by Poisson statistics, where the probability P_n of scattering is small in relation to the total number of events I, such that the average number of events P_n occurring is simply $\mu = P_n I$.

$$P_n = \frac{\mu^n e^{-\mu}}{n!} \tag{2.30}$$

The average number of events μ is determined by the *scattering parameter* t/λ where t is the sample thickness and λ the *mean free path* or the average distance between collisions. Replacing μ by t/λ, and given the initial intensity I:

$$I_n = IP_n = (I/n!)(t/\lambda)^n e^{-t/\lambda} \tag{2.31}$$

This is visualised in fig(2.11) which shows the probabilities of unscattered, single and double scattering events as a function of t/λ.

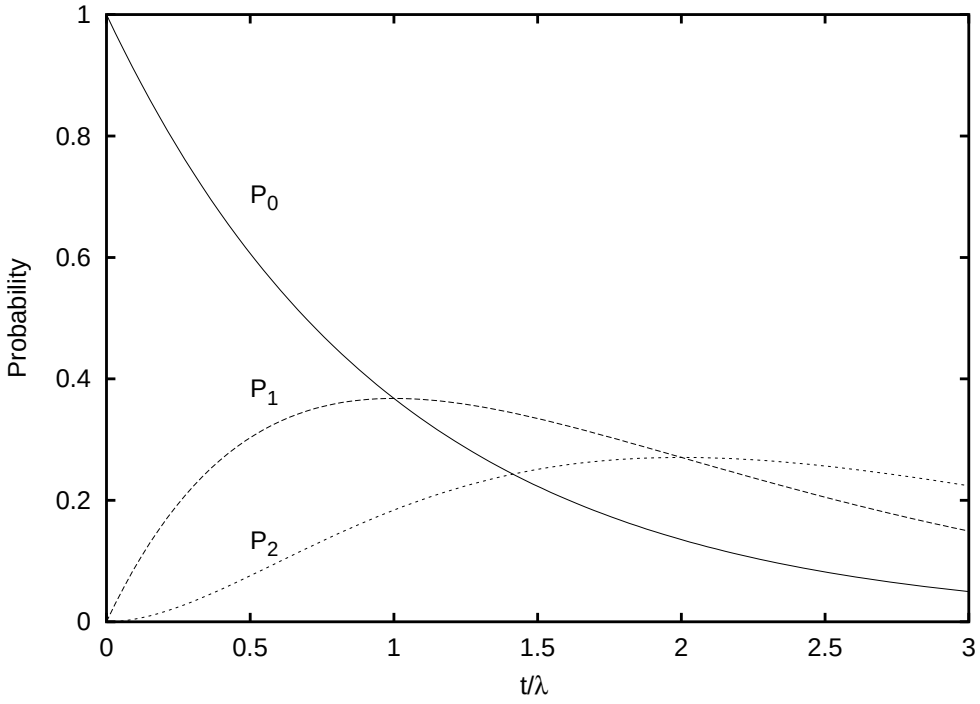

Figure 2.11: The probability of inelastic scattering as treated by Poisson statistics gives the probability of no inelastic collisions P_0, single scattering (P_1) and double scattering (P_2) as a function of t/λ, (t is the actual thickness, λ the mean-free-path), assuming no angle limiting aperture. Reproduced from Egerton [17]

The collected spectrum $J(E)$ is a sum of all components, unscattered, single, double, triple and so on. Their presence modifies the shape of core-loss edges and may lead to an incorrect calculation or interpretation of elemental composition. To remove these artefacts, two techniques are used, namely Fourier-Log and Fourier-Ratio deconvolution.

2.5.3 Fourier-Log Deconvolution

In the case of no scattering through a sample the collected spectrum $Z(E)$ will not be a delta function, but rather a convolution of the incident intensity and the instrumental resolution function $R(E)$, which is a unit-area function with a full-width at half-maximum of ΔE equal to the experimental resolution. Where :

$$Z(E) = I_0 R(E) \tag{2.32}$$

and from Eq.(2.31) I_0 is given by:

$$I_0 = I(t/\lambda)^0 e^{-t/\lambda} = I e^{-t/\lambda} \tag{2.33}$$

The single scattered distribution, for $n = 1$ is termed $S(E)$ is given by:

$$\int S(E)dE = I_1 = I/1!(t/\lambda)e^{-t/\lambda} = I_0/1!(t/\lambda) \tag{2.34}$$

Because of the instrumental resolution $R(E)$ we get the collected intensity $J^1(E)$ as a convolution of $S(E)$ and $R(E)$:

$$J^1(E) = S(E) * R(E) \tag{2.35}$$

Similarly the double scattered distribution $D(E)$ will give an experimental spectrum given by:

$$J^2(E) = D(E) * R(E) \tag{2.36}$$

The double scattered intensity will possess an energy dependence given by $S(E)*S(E)$, but with intensity I_2:

$$\int D(E)dE = I_2 = I/2!(t/\lambda)^2 e^{-t/\lambda} = I_0/2!(t/\lambda)^2 \tag{2.37}$$

It is clear that the area under $S(E)*S(E)$ will be proportional to $I_0^2(t/\lambda)^2$ [20] whereas the area under $D(E)$ should be $I_0/2!(t/\lambda)^2$, so a factor of $1/(I_0 2!)$ should be introduced giving $J^2(E)$ a dependence:

$$J^2(E) = D(E) * R(E) = R(E) * S(E) * S(E)/(I_0 2!) \tag{2.38}$$

Similarly the expression for $J^3(E)$ will involve the triple scattering term $T(E)$ and be:

$$J^3(E) = T(E) * R(E) = R(E) * S(E) * S(E) * S(E)/(I_0^2 3!) \tag{2.39}$$

The noise-free experimentally collected spectrum will therefore have the form:

$$\begin{aligned} J(E) &= J^0(E) + J^1(E) + J^2(E) + J^3(E) + \ldots \\ &= R(E) * (I_0\delta(E + S(E) + D(E) + T(E) + \ldots) \\ &= Z(E) * (\delta(E) + S(E)/I_0 + S(E) * S(E)/(I_0 2!) + \\ &\quad S(E) * S(E) * S(E)/(I_0^2 3!) + \ldots) \end{aligned} \tag{2.40}$$

The Fourier transform of $J(E)$ is given by:

$$j(\omega) = \int_{-\infty}^{\infty} J(E) e^{2\pi i \omega E} dE \tag{2.41}$$

By taking transforms of both sides of Eq.(2.40) the convolutions become products, and the Fourier transform of $\delta(E)$ is unity (in Fourier space) which leaves:

$$j(\omega) = z(\omega)\left[1 + s(\omega)/I_0 + s(\omega)^2/(I_0^2 2!) + s(\omega)^3/(I_0^3 3!) + \ldots\right] \tag{2.42}$$

As $e^x = 1 + x + x^2/2! + x^3/3! + \ldots$, we can rewrite Eq.(2.42) as:

$$j(\omega) = z(\omega)\left[e^{s(\omega)/I_0}\right] \tag{2.43}$$

by taking the natural logarithms of both sides produces:

$$s(\omega) = I_0 ln\left(\frac{j(\omega}{z(\omega)}\right) \tag{2.44}$$

where $s(\omega)$, $j(\omega)$ and $z(\omega)$ are the Fourier transforms of the single scattered, collected and zero-loss intensity respectively.

The recovery of the function S(E) should therefore involve the inverse Fourier transform of the expression in Eq.(2.44). This is complicated somewhat by the presence of noise in the collected spectrum which extends to all frequencies of $s(\omega)$, and also that $s(\omega)$ is finite in nature owing to the finite number of channels collected in the spectrum.

Noise is especially a problem in the evaluation of $ln(j(\omega)/z(\omega))$ especially at high ω where the signal to noise ratio is low.

Applying Fourier-Log deconvolution involves calculating the Fourier transform for the entire spectrum (low and core loss). Practical aspects of applying Fourier-Log deconvolution are discussed in detail by Egerton [17]. In this work, Fourier-ratio deconvolution was applied principally to determine the plasmon energy as a maximum in $S(E)$.

2.5.4 Fourier-Ratio Deconvolution

The Fourier-ratio technique is another method for deconvolution and uses a low-loss spectrum as a deconvolution function for the core-loss region. This is convenient in a practical sense as the low-loss and core-loss are generally collected separately. The technique essentially involves dividing the core-loss transform by the low-loss transform, as shown in the following:

$$k^1(\omega) = I_0 j_k(\omega)/j_l(\omega) \tag{2.45}$$

where the two measured spectra $j_k(\omega)$ and $j_l(\omega)$ are the core-loss and low-loss spectra respectively. Practical details of implementation to cope with noise and truncation of experimental spectra are discussed in Egerton [17]. The technique of Fourier-Ratio deconvolution was applied to all core-loss edges presented in Chapter 3.

2.5.5 Background fitting to Ionisation Edges

The onset of core-loss ionisation edges occurs at energies generally above 100eV as shown in Table 2.1. These features are on a monotonically decreasing background caused by the excitation of atomic electrons of lower binding energy or plasmon losses. This intensity must be removed before any quantitative elemental analysis can be performed and was used on all experimental core-loss spectra except those presented as integrated intensities in EELS line scans in Section 3.2 on page 65.

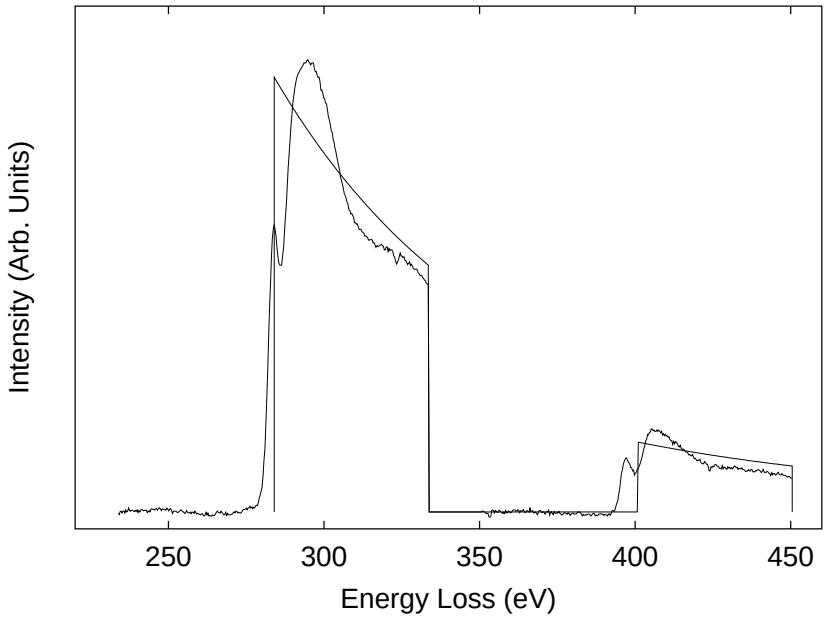

Figure 2.12: A typical fitting of hydrogenic cross-sections for a core-loss quantification of an amorphous carbon-nitride film.

The spectral intensity due to energy-loss processes are asymmetrical and have high energy tails which can be approximated to a power-law Ae^{-r}, where r is between 2-6, and is a function of specimen thickness, collection angle β and energy loss $E(eV)$. In practice, the function Ae^{-r} should be fitted to the spectrum as close as possible to the ionisation edge of interest. The fitting techniques used are least-squares χ^2 or the two-area method described in Egerton [17]. These were available in the processing package EL/P provided by Gatan.

2.5.6 Calculation of atomic concentration

The intensity alone of a core-loss spectral feature in EELS due to an element is not generally indicative of the amount of that element present in the sample. This is because the core-loss intensity is moderated by the elemental inelastic cross-section. The calculation of the inelastic cross-section is described by Bethe Theory in Eq. 2.26, in which a key quantity is the generalised oscillator strength (GOS). This is the response of an atom to energy and momentum supplied from an external source.

In a core-loss event, this includes the transition of the atom to an excited state, and

the transition of an electron from an initial to a final wavefunction. The initial and final wavefunctions for this process are calculated by using the Hydrogenic Model or Hartree-Slater Method.

For the Hydrogenic Model, initial and final wavefunctions are assumed to be "hydrogenic". That is, the wavefunctions are an exact solution to Schrödinger's equation:

$$(-\hbar^2/2m_0)\nabla^2\psi - (e^2/4\pi\varepsilon_0 r)\psi = E_t\psi$$

where E_t is the total energy of the electron (kinetic and electrostatic). To calculate accurate wavefunctions, the electrostatic energy (in E_t) is modified to account for the screening of nuclear charge by other electrons forming an *effective* nuclear charge.

The Hartree-Slater Method involves an iterative solution of the Schrödinger Equation until the electron density and electronic potential are self-consistent (Poisson's equation). The calculations for Hydrogenic or Hartree-Slater inelastic cross-sections are both available as Fortran programs from Egerton [17]. For light elements such as carbon and nitrogen, the Hydrogenic Model is of sufficient accuracy and gives good results.

The GOS is a function of energy loss E and momentum $\hbar q$ delivered to the atom. For a core-loss event this is a finite integral over a selected range of scattering angles and energy. Using Eq. (2.26) gives the partial cross-section for the element σ_k.

In practice, the core-loss intensity for each element is integrated in an energy "window" of width ΔE, and the partial inelastic cross-section σ_k calculated using the values of ΔE and incident angle α and collection angle β as shown in fig(2.13).

The integrated intensity I_k is therefore:

$$I_k(\beta, \Delta E) = N_k\sigma_k I_0(\beta, \Delta E) \tag{2.46}$$

where N_k is the number of atoms type k in the incident beam I_0. σ_k is the *cross-section* of the scattering event for the detector configuration.

For a sample containing two elements A & B, the atomic ratio (*ie.* the ratio of the

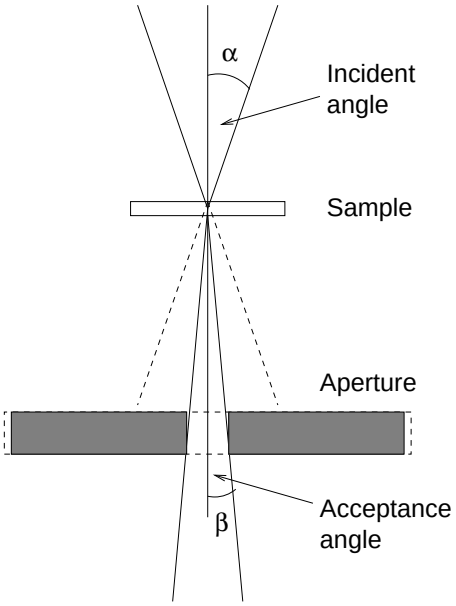

Figure 2.13: The incident and collected sub-angles α and β for energy loss spectroscopy.

number of atoms of each type present in the beam) is given by:

$$\frac{N_A}{N_B} = \frac{I_A(\beta, \Delta E)\sigma_B}{I_B(\beta, \Delta E)\sigma_A} \tag{2.47}$$

In practice, care must be taken to ensure samples measured using this technique are sufficiently thin to reduce contributions of multiple plasmon and plural scattering. This reduces the uncertainty in elemental concentration. Typically EELS elemental analysis is accurate to within $\pm 5\%$ if the integration window is >20eV [21].

2.5.7 Corrections for angles of incidence and collection

Electrons scattered inelastically from a specimen have a characteristic scattering angle θ_E of 5-10 mrad. For a parallel incident beam, there is a minor correction for the size of collection angle β as some electrons may be scattered to angles $> \beta$. For convergent incident beams, while $\alpha << \beta$ the quantification Eq.(2.47) is valid. As α increases, the likelihood that scattered electrons may not be collected also increases. This is especially true in scanning transmission electron microscopes where the beam is strongly convergent on the sample.

The correction factor replaces $I_k(\beta, \Delta)$ in Eq.(2.47) for $\alpha < \beta$:

$$\begin{aligned} I_k(\beta, \Delta) &= F_1 I_k(\alpha, \beta, \Delta) \\ F_1 &= \frac{2/\alpha^2}{ln[1 + (\beta/\theta_E)^2]} \int_0^\beta ln \left[\frac{\psi^2 + (\psi^4 + 4\theta^2\theta_E^2)^{1/2}}{2\theta_E^2} \right] \theta d\theta \end{aligned} \tag{2.48}$$

in which F_1 represents the reduction in collected intensity due to a large incident convergence angle. ψ is given by $\psi^2 = \alpha^2 + \theta_E^2 - \theta^2$ and θ_E the angular width of the Lorentzian core-loss function.

In situations where $\alpha > \beta$ another correction must be made, roughly approximated to the width of the convergent beam disk which falls upon the collection aperture, ie: proportional to $(\alpha/\beta)^2$. So in Eq.(2.48) above, F_1 should be replaced by $(\alpha/\beta)^2 F_1$.

Bibliography

[1] P. J. Martin, S. W. Filipczuk, R. P. Netterfield, J. S. Field, D. F. Whitnall, and D. R. McKenzie, Journal of Materials Science Letters **7,** 410–412 (1988).

[2] I. I. Aksenov, V. A. Belous, V. G. Padalka, and V. M. Khoroshikh, Soviet Journal Plasma Physics **4,** 425 (1978).

[3] E. G. Gerstner, Ph.D. thesis, University of Sydney, 1997.

[4] D. R. McKenzie, Rep. Prog. Phys. **59,** 1611–1664 (1996).

[5] M. K. Puchert, C. A. Davis, D. R. McKenzie, and B. W. James, Journal of Vacuum Science and Technology **A10,** 3493–3498 (1992).

[6] D. B. Williams and C. B. Carter, *Transmission Electron Microscopy* (Plenum Press, New York, 1996).

[7] *CRC Handbook of Chemistry and Physics*, 73rd ed., D. R. Lide, ed., (CRC Press Inc. Ann Arbor, 1992–93).

[8] J. M. Cowley, *Diffraction Physics* (North Holland Publishing Company, 1975).

[9] D. J. H. Cockayne and D. R. McKenzie, Acta Crystallographica **A44,** 870 (1988).

[10] *X-Ray Diffraction*, B. E. Warren, ed., (Addison-Wesley Publishing Company, Reading MA, 1969).

[11] D. J. H. Cockayne, D. R. McKenzie, and D. A. Muller, Microscopy, Microanalysis and Microstructure **2,** 359–366 (1991).

[12] D. A. Muller, Master's thesis, School of Physics, University of Sydney, 1993.

[13] W. E. McBride, Ph.D. thesis, University of Sydney, 2000.

[14] D. G. McCulloch, D. R. McKenzie, C. M. Goringe, D. J. H. Cockayne, W. E. McBride, and D. C. Green, Acta Crystallographica **A55,** 178–187 (1999).

[15] G. Ruthemann, Naturwissenschaften **29,** 648 (1941).

[16] J. Hillier and R. F. Baker, Physical Review **64,** 318–319 (1944).

[17] R. F. Egerton, *Electron Energy Loss Spectroscopy in the Electron Microscope*, 2nd ed. (Plenum Press New York, 1996).

[18] S. D. Berger, D. R. McKenzie, and P. J. Martin, Philosophical Magazine Letters **57,** 285 (1988).

[19] D. G. McCulloch, D. R. McKenzie, and C. M. Goringe, Physical Review B **61,** 2349–2355 (2000).

[20] R. N. Bracewell, *The Fourier Transform and its Applications*, 2nd ed. (McGraw Hill Book Company, New York, 1986).

[21] X. Weng and P. Rez, Ultramicroscopy **25,** 345–348 (1988).